3-D FE Discontinuous Sheet for Microwave Heating

Richard A. Ehlers, *Member, IEEE,* and A. C. Ricky Metaxas, *Member, IEEE*

***Abstract*—This paper presents a method for modeling the electromagnetic properties of thin metallic films typical of electromagnetically active food packages within multimode microwave applicators. A discontinuous sheet with six degrees of freedom (DOF) is incorporated within a time- or frequency-domain edge finite-element formulation by splitting the tetrahedral-element discretized domain on the thin-film surface and adding new DOF. Superior accuracy is observed when comparing with existing surface sheet conditions. Thermal image validation is provided for multimode applications.**

***Index Terms*—Finite edge element, metallic sheet, microwave package, thin conducting film.**

I. INTRODUCTION

THE use of the approximate boundary conditions such as the standard impedance boundary condition (SIBC) proposed by Leontovich [1] have seen extensive use in electromagnetic (EM) applications for many years. Although these conditions are satisfactory for representing highly reflective surfaces, they fail as the surface becomes more transmissive. The resistive sheet [2] and the so-called modified resistive sheet [3] are, however, able to account for the transmitted field component, although with a loss in accuracy, as will be shown. Improved accuracy is brought about by making use of a dual-surface method, which has been seen for the finite difference time domain (FDTD) [4], as well as for a two-dimensional (2-D) finite-element (FE) application [5]. However, no application of a dual-surface method for modeling thin films using the FE method has been seen as three-dimensional (3-D). Hence, the focus of this paper is to introduce such a method and present results of its application within a microwave heating context [6].

II. THIN-FILM BOUNDARY CONDITIONS

The impedance as used in a modification of the SIBC extended to incorporate the film thickness τ is given as [7]

$$Z_{\text{in}} = Z_f \frac{Z_0 + Z_f \tanh(\gamma_1 \tau)}{Z_f + Z_0 \tanh(\gamma_1 \tau)} \ (\Omega) \tag{1}$$

where the film impedance Z_f for a conductivity σ_f is defined as

$$Z_f = (1+\jmath)\sqrt{\frac{\omega\mu}{2\sigma_f}} \ (\Omega). \tag{2}$$

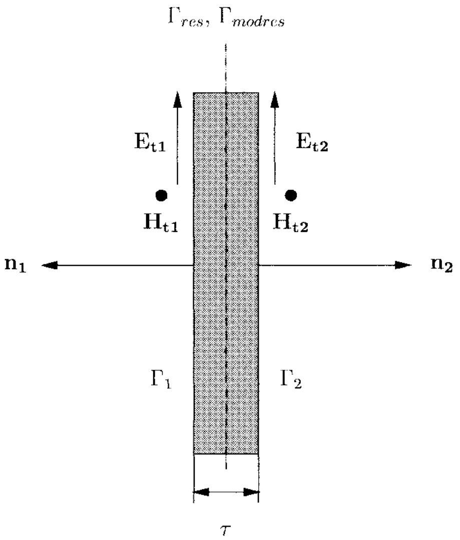

Fig. 1. Tangential-field components either side of a thin-film surface, as used in the resistive, modified resistive, and discontinuous sheets.

The complex propagation constant for a nonmagnetic metal is expanded, with f being the frequency, as

$$\gamma_1 = (1+\jmath)\sqrt{\pi\mu_0 f \sigma_f} \ (\text{m}^{-1}). \tag{3}$$

With reference to Fig. 1, alternative thin-film boundary conditions are described. The resistive sheet condition, which assumes continuity in the tangential electric field $E_{t1} = E_{t2}$ is

$$\mathbf{n}\times\mathbf{n}\times\mathbf{E} = -Z_{\text{res}}[\mathbf{n}\times\mathbf{H}]_-^+ \tag{4}$$

where Z_{res} is the sheet impedance given by

$$Z_{\text{res}} = \frac{-\jmath}{\omega\epsilon_0\tau(\epsilon_r - 1)} \ (\Omega) \tag{5}$$

and the permittivity is expanded as $\epsilon_r = \epsilon' - \jmath\epsilon''$, in which ϵ'' is understood to represent all possible material losses. In the modified resistive sheet, the discontinuity in the electric field is accounted for, i.e., $E_{t1} \neq E_{t2}$

$$\mathbf{E_{t2}} = \alpha\mathbf{E_{t1}} \tag{6}$$

where

$$\alpha = \cos(\gamma_2\tau) + \frac{1}{Z_0}\left(\frac{\jmath\omega\mu}{\gamma_2}\right)\sin(\gamma_2\tau) \tag{7}$$

and $\gamma_2 = \omega\sqrt{\mu\epsilon_0\epsilon_r}$.

Unlike any of the methods already described where the same surface (Γ_{res} or Γ_{modres}) represents components of incident and transmitted fields, the discontinuous sheet introduces additional

Manuscript received October 16, 2001; revised September 6, 2002.

The authors are with the Electricity Utilization Group, Engineering Department, University of Cambridge, Cambridge CB2 1PZ, U.K. (e-mail: rae@cantab.net; acm@metaxas-associates.com).

Digital Object Identifier 10.1109/TMTT.2003.808731

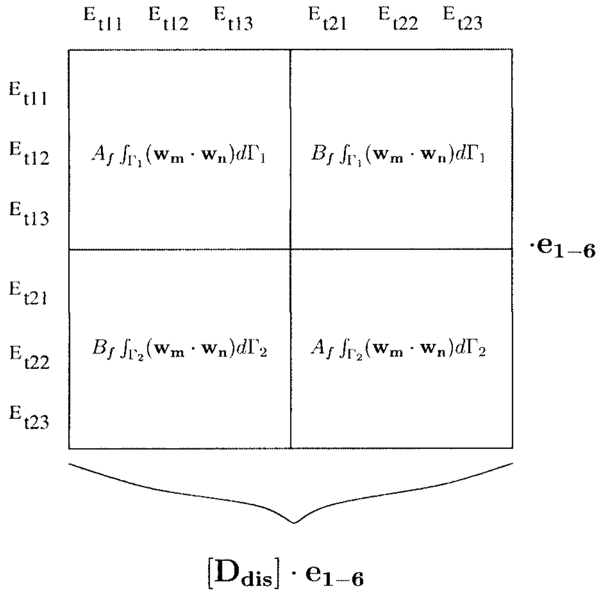

Fig. 2. Thin-film element matrix used for the frequency-domain discontinuous sheet.

degrees of freedom (DOF) by way of a dual surface (Γ_1 and Γ_2) representation of the thin-film surface where the following transmission-line equalities hold:

$$\begin{bmatrix}\mathbf{E_{t1}}\\ \mathbf{E_{t2}}\end{bmatrix}=\begin{bmatrix}Z_{11} & -Z_{12}\\ Z_{12} & -Z_{11}\end{bmatrix}\begin{bmatrix}\mathbf{n_1}\times\mathbf{H_{t1}}\\ \mathbf{n_2}\times\mathbf{H_{t2}}\end{bmatrix}. \tag{8}$$

The impedances Z_{11} and Z_{12} are given as [4]

$$Z_{11}=\frac{-j\omega\mu}{\gamma_2\tan(\gamma_2\tau)}\text{ and }Z_{12}=\frac{-j\omega\mu}{\gamma_2\sin(\gamma_2\tau)}. \tag{9}$$

The numerical implementation of the discontinuous sheet is discussed below for both the frequency and time domains where all mediums are considered to be homogeneous. The implementation requires that the mesh representing the computation domain is split on the relevant thin-film structure(s) such that the film surface can be duplicated, creating additional DOF. Two surface integral terms are required within the numerical formulation, each of which is responsible for modeling the tangential-field components on one of the two surfaces resulting from the split mesh. To link the mesh again, a thin-film element of the discontinuous sheet is thus required to have six DOF—three for each surface integral term.

III. FREQUENCY-DOMAIN FORMULATION

Equation (8) can be rewritten in terms of the magnetic-field components as

$$\begin{bmatrix}\mathbf{n_1}\times\mathbf{H_1}\\ \mathbf{n_2}\times\mathbf{H_2}\end{bmatrix}=\begin{bmatrix}\dfrac{Z_{11}}{Z_{11}^2-Z_{12}^2} & \dfrac{-Z_{12}}{Z_{11}^2-Z_{12}^2}\\ \dfrac{-Z_{12}}{Z_{11}^2-Z_{12}^2} & \dfrac{Z_{11}}{Z_{11}^2-Z_{12}^2}\end{bmatrix}\begin{bmatrix}\mathbf{E_{t1}}\\ \mathbf{E_{t2}}\end{bmatrix}. \tag{10}$$

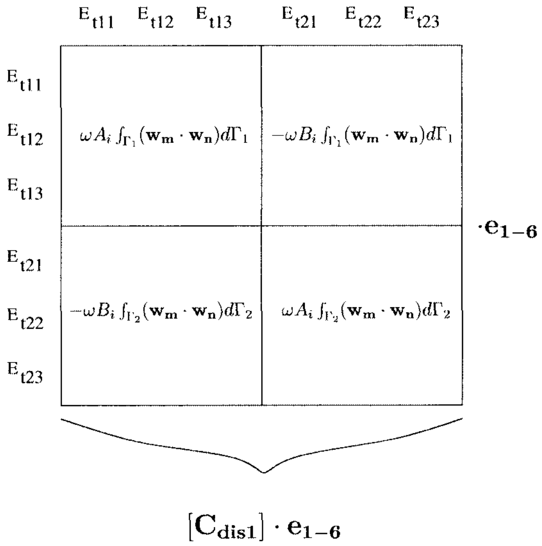

Fig. 3. Thin-film elemental matrix with no field temporal derivative term used for the time-domain discontinuous sheet.

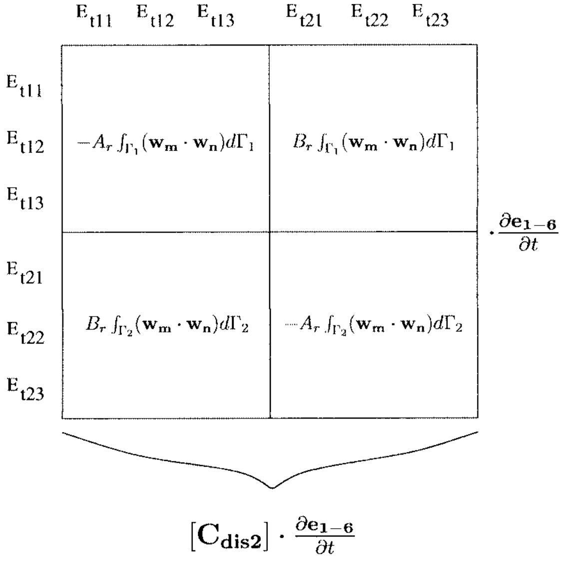

Fig. 4. Thin-film elemental matrix with field first temporal derivative term used for the time —domain discontinuous sheet.

Manipulating Maxwell's equation, the Helmholtz equation is derived, which is then modified to include two surface integrals as follows:

$$\begin{aligned}\frac{1}{\mu}\int_\Omega(\nabla\times\psi)\cdot(\nabla\times\mathbf{E})d\Omega-\omega^2\epsilon_0\epsilon_r\int_\Omega\psi\cdot\mathbf{E}d\Omega\\ =-j\omega\int_\Omega\psi\cdot\mathbf{J_s}+j\omega\int_{\Gamma1}\psi\cdot(\mathbf{n_1}\times\mathbf{H_{t1}})d\Gamma1\\ +j\omega\int_{\Gamma2}\psi\cdot(\mathbf{n_2}\times\mathbf{H_{t2}})d\Gamma2\end{aligned} \tag{11}$$

where $\mathbf{J_s}$ represents the microwave cavity source excitation. Substituting (10) into (11) and making use of edge elements, the frequency-domain edge element discretized formulation including the discontinuous sheet is

$$[\mathbf{S}]\mathbf{e}-\gamma_0^2[\mathbf{T}]\mathbf{e}-[\mathbf{D}_{\text{dis}}]\mathbf{e}=\mathbf{b} \tag{12}$$

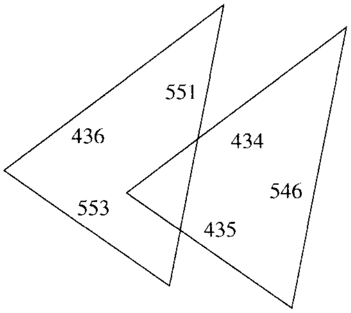

Fig. 5. Pure discontinuous sheet element. The numbers beside each edge are random and represent typical global matrix edge index entries.

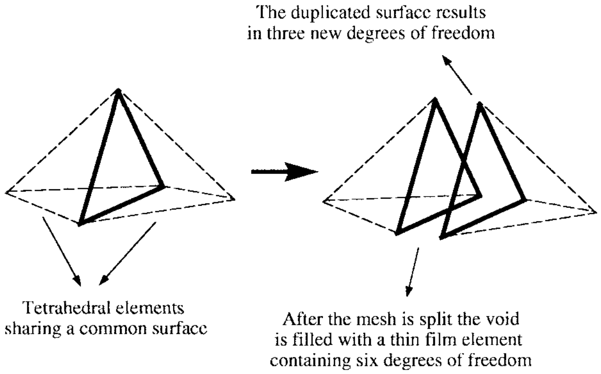

Fig. 6. Splitting of a tetrahedral mesh to include a thin-film element.

where the stiffness and mass matrices are represented by $[\mathbf{S}]$ and $[\mathbf{T}]$, respectively, $\mathbf{e}$ is the vector of unknown edge values, and $\mathbf{b}$ denotes the source vector. The matrix $\mathbf{D}_{\rm dis}$ represents the surface integrals of (11) and is expanded together with the electric field as

$$[\mathbf{D}_{\rm dis}]\mathbf{e} = [\mathbf{D_1}]\mathbf{e_{1-3}} - [\mathbf{D_2}]\mathbf{e_{4-6}} - [\mathbf{D_3}]\mathbf{e_{1-3}} + [\mathbf{D_4}]\mathbf{e_{4-6}}. \tag{13}$$

The matrix and vector entries corresponding to an individual element are

$$[\mathbf{D_1}]^e_{m,n} e_m{}^e = \frac{\jmath\omega Z_{11}}{Z_{11}^2 - Z_{12}^2}\int_{\Gamma 1}(\mathbf{w_{1-3}}\cdot\mathbf{w_{1-3}})\mathbf{e_{1-3}}\,d\Gamma 1 \tag{14}$$

$$[\mathbf{D_2}]^e_{m,n} e_m{}^e = -\frac{\jmath\omega Z_{12}}{Z_{11}^2 - Z_{12}^2}\int_{\Gamma 1}(\mathbf{w_{1-3}}\cdot\mathbf{w_{4-6}})\mathbf{e_{4-6}}\,d\Gamma 1 \tag{15}$$

$$[\mathbf{D_3}]^e_{m,n} e_m{}^e = -\frac{\jmath\omega Z_{12}}{Z_{11}^2 - Z_{12}^2}\int_{\Gamma 2}(\mathbf{w_{4-6}}\cdot\mathbf{w_{1-3}})\mathbf{e_{1-3}}\,d\Gamma 2 \tag{16}$$

$$[\mathbf{D_4}]^e_{m,n} e_m{}^e = \frac{\jmath\omega Z_{11}}{Z_{11}^2 - Z_{12}^2}\int_{\Gamma 2}(\mathbf{w_{4-6}}\cdot\mathbf{w_{4-6}})\mathbf{e_{4-6}}\,d\Gamma 2 \tag{17}$$

where $\mathbf{e_{1-3}}$ and $\mathbf{e_{4-6}}$ are vector entries of the electric-field circulation on each of the two triangular surfaces of the thin-film element. The corresponding basis functions are given by $\mathbf{w_{1-3}}$ and $\mathbf{w_{4-6}}$, respectively.

The thin-film element consists of a single matrix comprised of contributions from each of the four matrices and corresponding vector entries, from (13), with a total of six DOF, as shown in Fig. 2. The coefficients in Fig. 2 are given as

	1	2	3	4	5	6	
1	A	A	A	-B	-B	-B	e1
2	A	A	A	-B	-B	-B	e2
3	A	A	A	-B	-B	-B	e3
4	-B	-B	-B	A	A	A	e4
5	-B	-B	-B	A	A	A	e5
6	-B	-B	-B	A	A	A	e6

Fig. 7. Pure discontinuous sheet element impedance matrix showing link between the edge components. The numbers 1–6 denote the matrix row and column indexes.

	434	435	436	546	551	553
434	A	A	-B	A	-B	-B
435	A	A	-B	A	-B	-B
436	-B	-B	A	-B	A	A
546	A	A	-B	A	-B	-B
551	-B	-B	A	-B	A	A
553	-B	-B	A	-B	A	A

Fig. 8. Typical global matrix entries for a film element configuration shown in Fig. 5.

$$A_f = \frac{\jmath\omega Z_{11}}{Z_{11}^2 - Z_{12}^2} \text{ and } B_f = -\frac{\jmath\omega Z_{12}}{Z_{11}^2 - Z_{12}^2}. \tag{18}$$

In Figs. 2–4, $\mathbf{w_m}$ and $\mathbf{w_n}$ correspond to the basis functions of edges m and n, respectively. Furthermore, the tangential electric field indexes on the two surfaces of the thin-film element are given by $E_{t1(1-3)}$ and $E_{t2(1-3)}$.

IV. Time-Domain Formulation

The wave equation, which is derived from Maxwell's equations in the time domain, is supplemented with two surface integral terms Γ_1 and Γ_2, which are required for the discontinuous sheet. The use of a first-order absorbing boundary condition (ABC) is adopted in the time domain in order to represent an iso-circulator that protects the magnetron source from cavity reflections. The ABC is evaluated by adding an

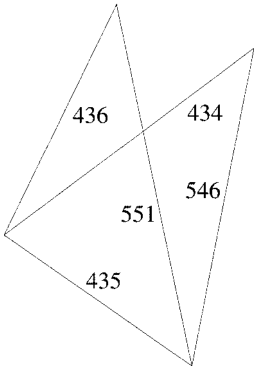

Fig. 9. Hybrid discontinuous-resistive sheet element. The numbers beside each edge are random and represent typical global matrix edge index entries.

	1	2	3	4	5	6	
1	R/2	$\frac{A-B}{2}$	$\frac{A-B}{2}$	R/2	$\frac{A-B}{2}$	$\frac{A-B}{2}$	e1
2	$\frac{A-B}{2}$	A	A	$\frac{A-B}{2}$	-B	-B	e2
3	$\frac{A-B}{2}$	A	A	$\frac{A-B}{2}$	-B	-B	e3
4	R/2	$\frac{A-B}{2}$	$\frac{A-B}{2}$	R/2	$\frac{A-B}{2}$	$\frac{A-B}{2}$	e4
5	$\frac{A-B}{2}$	-B	-B	$\frac{A-B}{2}$	A	A	e5
6	$\frac{A-B}{2}$	-B	-B	$\frac{A-B}{2}$	A	A	e6

Fig. 10. Hybrid discontinuous-resistive film element impedance matrix used on the film boundary. The numbers 1–6 denote the matrix row and column indexes.

additional surface integral term Γ_{ABC}, to the wave equation [11]

$$\begin{aligned}&\frac{1}{\mu}\int_{\Omega}(\nabla\times\psi)\cdot(\nabla\times\mathbf{E})d\Omega+\sigma\int_{\Omega}\psi\cdot\frac{\partial\mathbf{E}}{\partial t}d\Omega\\&\quad+\epsilon_0\epsilon'\int_{\Omega}\psi\cdot\frac{\partial^2\mathbf{E}}{\partial t^2}d\Omega-\int_{\Gamma 1}\psi\cdot(\mathbf{n_1}\times\jmath\omega\mathbf{H_{t1}})d\Gamma_1\\&\quad-\int_{\Gamma 2}\psi\cdot(\mathbf{n_2}\times\jmath\omega\mathbf{H_{t2}})d\Gamma_2\\&\quad=-\int_{\Omega}\psi\cdot\frac{\partial\mathbf{J_s}}{\partial t}d\Omega+\int_{\Gamma_{\mathrm{ABC}}}\psi\cdot\left(\mathbf{n}\times\frac{\partial\mathbf{H}}{\partial t}\right)d\Gamma_{\mathrm{ABC}}\end{aligned}\tag{19}$$

where σ is understood to describe both the conductive and dipolar loss mechanisms within the dielectric material. Substituting for the electric field from the discontinuous sheet condition in (10), the surface integrals Γ_1 and Γ_2, shown in the above equation, are rewritten as

$$\begin{aligned}&-\int_{\Gamma_1}\psi\cdot A_f\mathbf{E_{t1}}d\Gamma_1-\int_{\Gamma_1}\psi\cdot B_f\mathbf{E_{t2}}d\Gamma_1\\&\quad-\int_{\Gamma_2}\psi\cdot B_f\mathbf{E_{t1}}d\Gamma_2-\int_{\Gamma_2}\psi\cdot A_f\mathbf{E_{t2}}d\Gamma_2\end{aligned}\tag{20}$$

	434	435	436	546	551
434	A	A-B	-B	A	-B
435	A-B	2R	A-B	A-B	A-B
436	-B	A-B	A	-B	A
546	A	A-B	-B	A	-B
551	-B	A-B	A	-B	A

Fig. 11. Typical global matrix entries for a film boundary element configuration shown in Fig. 9.

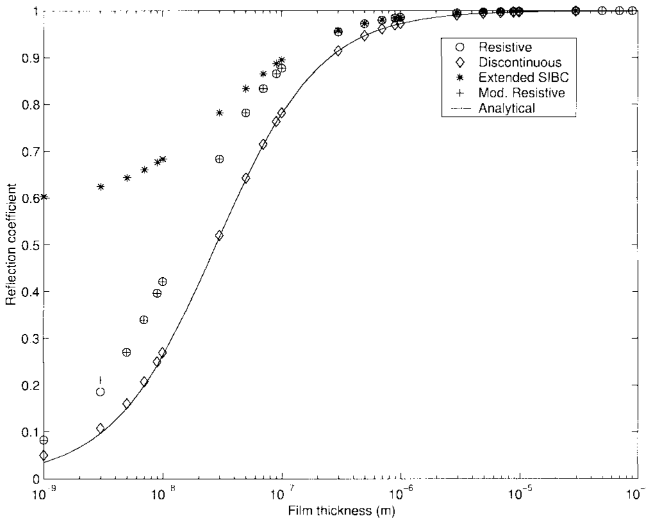

Fig. 12. Comparison of the extended SIBC, resistive sheet, modified resistive sheet, and discontinuous sheet with the analytical equivalent.

where A_f and B_f are the complex coefficients given by (18), which can be separated into real (A_r and B_r) and imaginary (A_i and B_i) components

$$\begin{aligned}&-\int_{\Gamma_1}\psi\cdot\jmath\omega\left(A_r+\jmath\omega\frac{A_i}{\omega}\right)\mathbf{E_{t1}}d\Gamma_1\\&+\int_{\Gamma_1}\psi\cdot\jmath\omega\left(B_r+\jmath\omega\frac{B_i}{\omega}\right)\mathbf{E_{t2}}d\Gamma_1\\&+\int_{\Gamma_2}\psi\cdot\jmath\omega\left(B_r+\jmath\omega\frac{B_i}{\omega}\right)\mathbf{E_{t1}}d\Gamma_2\\&-\int_{\Gamma_2}\psi\cdot\jmath\omega\left(A_r+\jmath\omega\frac{A_i}{\omega}\right)\mathbf{E_{t2}}d\Gamma_2.\end{aligned}\tag{21}$$

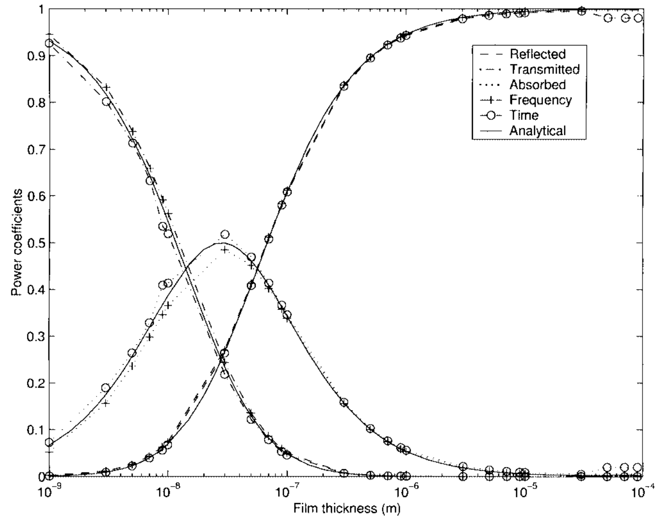

Fig. 13. Power coefficients of the discontinuous sheet as a function of thin-film thickness.

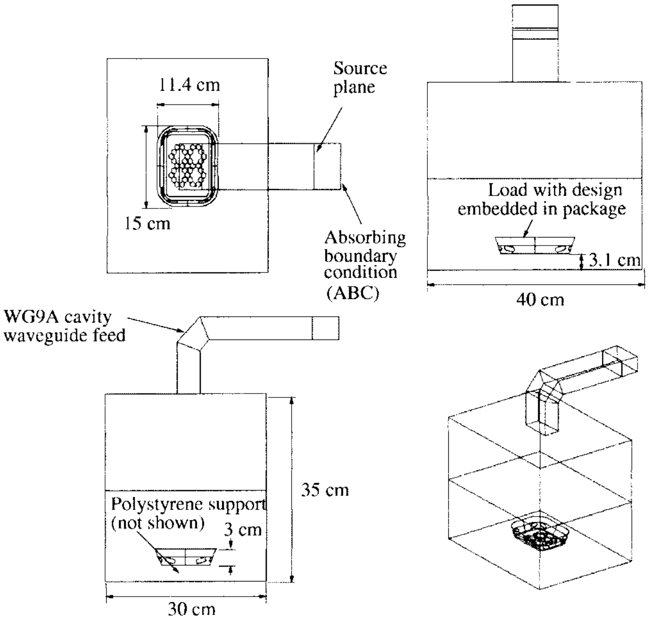

Fig. 14. Multimode oven setup used for experimental and numerical analysis.

Since the cavity excitation and operation is at a single frequency, the coefficients A_r, B_r, A_i, and B_i are constants. Transforming to the time domain yields

$$\begin{aligned}&-A_r\int_{\Gamma_1}\psi\cdot\frac{\partial\mathbf{E_{t1}}}{\partial t}d\Gamma_1+B_r\int_{\Gamma_1}\psi\cdot\frac{\partial\mathbf{E_{t2}}}{\partial t}d\Gamma_1\\&+A_i\int_{\Gamma_1}\psi\cdot\omega\mathbf{E_{t1}}d\Gamma_1-B_i\int_{\Gamma_1}\psi\cdot\omega\mathbf{E_{t2}}d\Gamma_1\\&+B_r\int_{\Gamma_2}\psi\cdot\frac{\partial\mathbf{E_{t1}}}{\partial t}d\Gamma_2-A_r\int_{\Gamma_2}\psi\cdot\frac{\partial\mathbf{E_{t2}}}{\partial t}d\Gamma_2\\&-B_i\int_{\Gamma_2}\psi\cdot\omega\mathbf{E_{t1}}d\Gamma_2+A_i\int_{\Gamma_2}\psi\cdot\omega\mathbf{E_{t2}}d\Gamma_2. \qquad (22)\end{aligned}$$

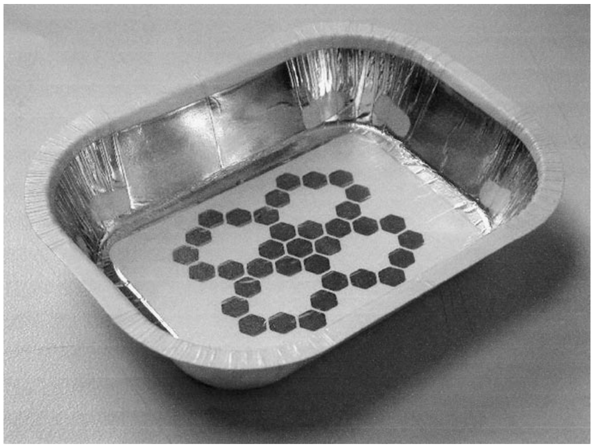

Fig. 15. Food package design with open-circuited antenna base pattern.

where the constant ω represents the fixed operating frequency. Discretizing using edge elements, the time-domain matrix representation including the discontinuous sheet is

$$\begin{aligned}&[\mathbf{S}]\mathbf{e}+[\mathbf{T}_\sigma]\frac{\partial\mathbf{e}}{\partial t}+[\mathbf{T}_\epsilon]\frac{\partial^2\mathbf{e}}{\partial t^2}\\&\quad+[\mathbf{C}_{\mathrm{ABC}}]\frac{\partial\mathbf{e}}{\partial t}+[\mathbf{C}_{\mathrm{dis1}}]\mathbf{e}+[\mathbf{C}_{\mathrm{dis2}}]\frac{\partial\mathbf{e}}{\partial t}=\mathbf{b} \qquad (23)\end{aligned}$$

where $[\mathbf{S}]$ is the stiffness matrix, $[\mathbf{T}_\sigma]$ together with $[\mathbf{T}_\epsilon]$ represent the mass matrices, and $[\mathbf{C}_{\mathrm{ABC}}]$ denotes the contribution of the absorbing boundary. The thin-film matrices $[\mathbf{C}_{\mathrm{dis1}}]$ and $[\mathbf{C}_{\mathrm{dis2}}]$ are assembled using (22) and are shown together with their corresponding electric-field edge value terms in Figs. 3 and 4, respectively [9]. The elemental matrices have six DOF, three for each surface, assuming a tetrahedral mesh is used. For each thin-film element, two elemental matrices are added to the global matrix. Using the Newmark time-stepping method [10], the film element entries $[\mathbf{C}_{\mathrm{dis1}}]$ and $[\mathbf{C}_{\mathrm{dis2}}]$ for the field at the current time step, denoted by subscript $n+1$, and its relation to the previous two time steps, denoted by subscripts n and $n-1$, are added to the existing scheme as

$$\begin{aligned}&\Big[[\mathbf{T}_\epsilon]+\gamma_t\Delta t\big([\mathbf{T}_\sigma]+[\mathbf{C}_{\mathrm{dis2}}]\big)+\beta_t\Delta t^2\big([\mathbf{S}]+[\mathbf{C}_{\mathrm{dis1}}]\big)\Big]\mathbf{e_{n+1}}\\&\quad=\Big[2[\mathbf{T}_\epsilon]-(1-2\gamma_t)\Delta t\big([\mathbf{T}_\sigma]+[\mathbf{C}_{\mathrm{dis2}}]\big)\\&\qquad-(0.5+\gamma_t-2\beta_t)\Delta t^2\big([\mathbf{S}]+[\mathbf{C}_{\mathrm{dis1}}]\big)\Big]\mathbf{e_n}\\&\qquad+\Big[-[\mathbf{T}_\epsilon]-(\gamma_t-1)\Delta t\big([\mathbf{T}_\sigma]+[\mathbf{C}_{\mathrm{dis2}}]\big)\\&\qquad-(0.5+\gamma_t+\beta_t)\Delta t^2\big([\mathbf{S}]+[\mathbf{C}_{\mathrm{dis1}}]\big)\Big]\mathbf{e_{n-1}}\\&\qquad+\Delta t^2\big[\beta_t\mathbf{b_{n+1}}+(0.5+\gamma_t-2\beta_t)\mathbf{b_n}\\&\qquad\quad+(0.5-\gamma_t+\beta_t)\mathbf{b_{n-1}}\big] \qquad (24)\end{aligned}$$

where the Newmark parameters $\beta_t=0.25$ and $\gamma_t=0.5$ are chosen to provide unconditional stability [8]. The use of (22) relies on the fact that a single operating frequency is used in the oven. The justification for the time-domain implementation of the discontinuous sheet is due to the fact that the time domain is able to deal faster and more efficiently with the ill-conditioned matrices arising from multimode applicator heating problems than the frequency domain [8].

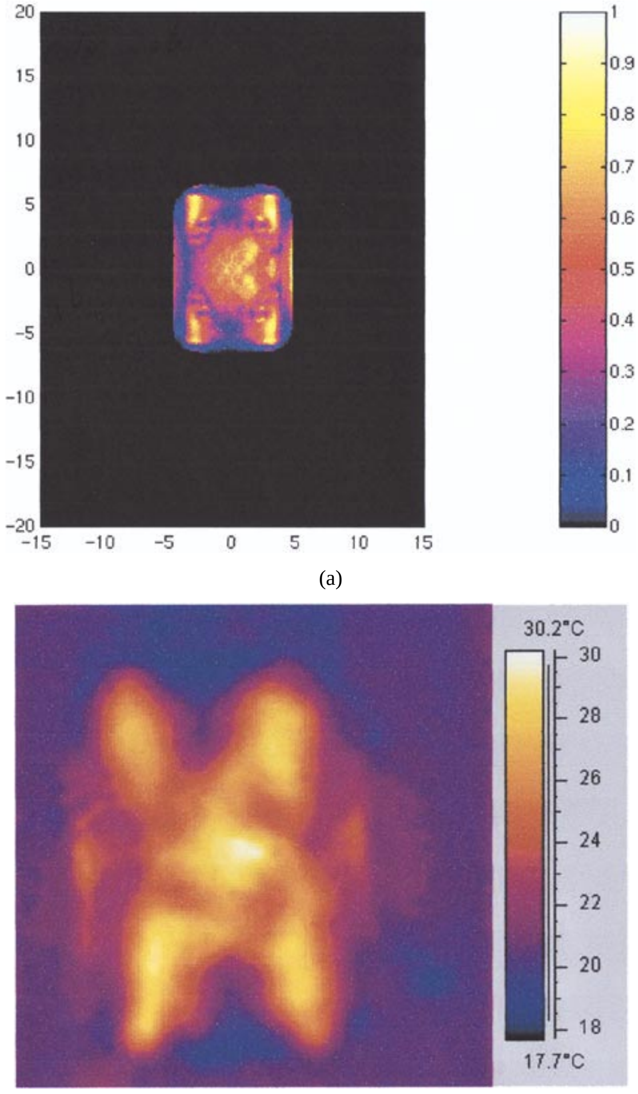

(a)

(b)

Fig. 16. Food surface plot at the base of the aluminum film package shown in Fig. 15. (a) Numerical. (b) Thermal image.

Fig. 17. Food package design with shielding in base pattern.

V. IMPLEMENTATION

Fig. 5 depicts the global numbering of a split surface as is required for a discontinuous sheet implementation. The process of splitting a mesh on a surface that belongs to two tetrahedral elements in order to include a thin-film element is depicted in Fig. 6. The impedance weighting, denoted by the variables A

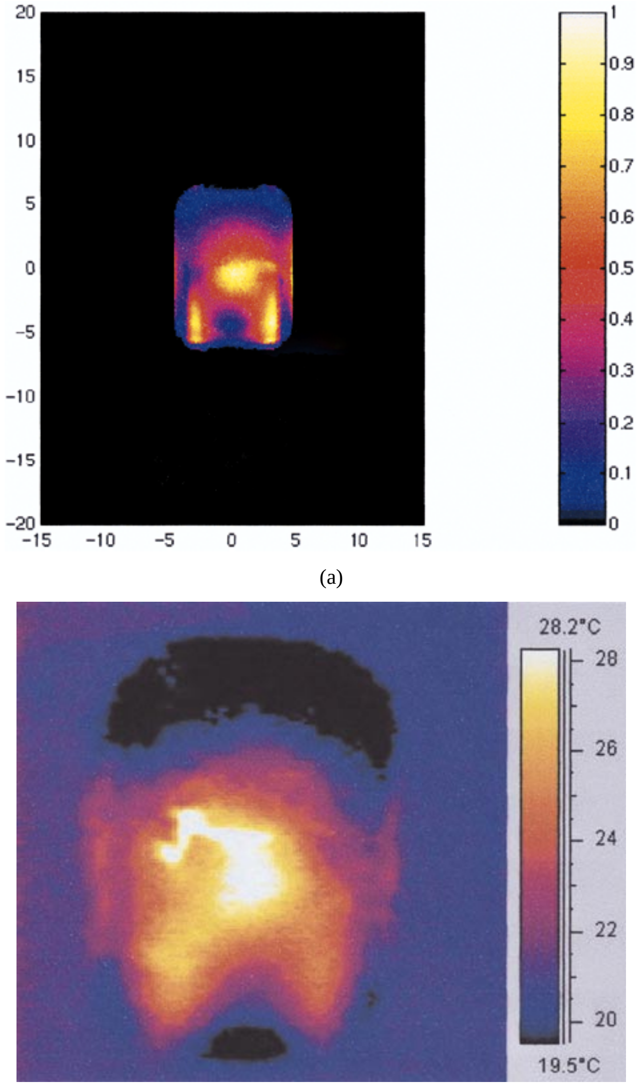

(a)

(b)

Fig. 18. Food surface plot at the base of the aluminum film package shown in Fig. 17. (a) Numerical. (b) Thermal image.

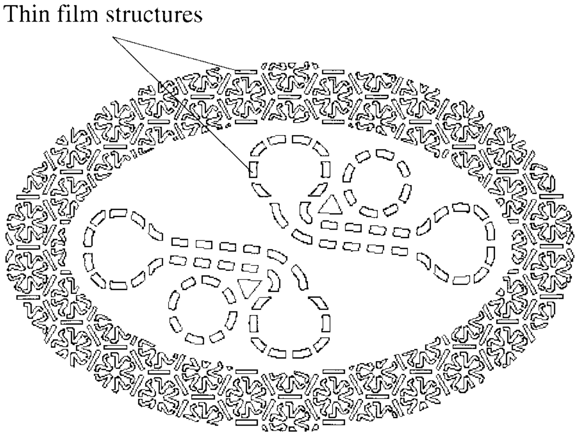

Fig. 19. Pattern of metallic antenna structures.

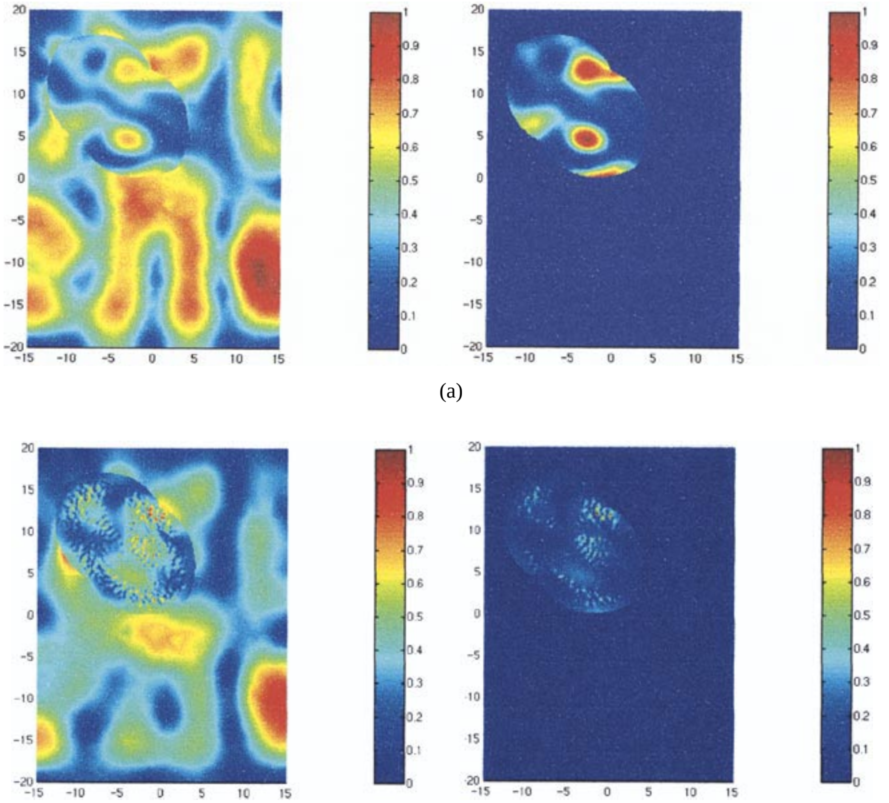

(a)

(b)

Fig. 20. Normalized absolute electric field (*left*) and power density patter (*right*) on a plane through the multimode applicator (Fig. 14) that is coincident with the butter load surface for: (a) without thin-film surface and (b) with thin-film surface.

and B, of the thin-film element used to fill the void is shown in Fig. 7 together with the six DOF ($e1$–$e6$) that correspond to the edges of both surfaces in Fig. 5. These variables A and B were defined in Fig. 2 for the frequency domain and Figs. 3 and 4 for the time domain, where A denotes the top left-hand-side and bottom right-hand-side matrix entries and B denotes the top right-hand-side and bottom left-hand-side entries. The global matrix contributions of these impedance coefficients are shown for the respective DOF in Fig. 8. Such an implementation for a thin-film element constitutes a pure discontinuous application.

Where the geometry adopting the thin-film surface is coupled to the surrounding mesh structure, a common DOF is required, as shown in Fig. 9. The latter describes the use of a hybrid discontinuous-resistive sheet, where the impedance weighting of the common edge R corresponds to that of a resistive sheet. A typical thin-film element impedance matrix for such a hybrid sheet is shown in Fig. 10, where the global matrix contributions are shown in Fig. 11.

VI. RESULTS

A. Analytical: Forward-Traveling Waveguide

Validation is obtained using analytical expressions within a forward-traveling WG9A waveguide ($x = 8.6$ cm $\times$ $y = 4.3$ cm $\times$ $z = 40$ cm) operating at 2450 MHz [12]. A thin film is placed midway ($z = 20$ cm) between the source ($z = 0$ cm) and a reflectionless termination to the waveguide ($z = 40$ cm). The reflection coefficient is compared with each of the four boundary methods discussed in Section II using a range of film thicknesses constituting reflective and transparent thin-film properties. These are shown for a film of conductivity 1.326e5 S/m in Fig. 12. The superior performance of the discontinuous sheet is evident, which is shown with reflected, absorbed, and transmitted power coefficients in Fig. 13.

B. Thermal Imaging: Multimode Resonant Applicator

With the lack of available analytical expressions to accurately represent a multimode heating system, a thermal imaging technique is used for validation. An image of the radiated thermal energy from the surface of an experimentally heated load is used as a qualitative representation of the dissipated power within the load. This can be compared with load surface power density obtained from the numerical result for the electric-field distribution. All numerical simulations are carried out on a Pentium II 450-MHz processor. Three active package configurations, using aluminum foil (3.77e7 S/m) of thickness 6.4 μm, are considered in a multimode cavity, where the setup for the first configuration is shown in Fig. 14. Other film thicknesses and conductivities may also be used depending on the application for which the thin film is required. The thin-film substrate provides structural support, but it is not modeled, as it is assumed to be microwave transparent. The active pack, as seen from Fig. 15, provides shielding on the package sidewalls and an antenna pattern arrangement at the base that is open circuited for safety precautions when the package is unloaded. When loaded with a food product such as mashed potato $(55 - \jmath 26.5)$, these structures are linked together using the ionic properties of the load. The resulting pattern at the base of the package is shown for the numerical power density and experimental thermal image in Fig. 16. The numerical result, which consisted of 684 955 DOF, was obtained after 32 h and 30 min using a convergence criterion of 4% change between successive cycles in the time domain.

The second configuration is aimed at studying the shielding performance of the package in Fig. 17, where half of the base is shielded for protecting microwave sensitive loads, while loads requiring more exposure to microwave energy are placed in the unshielded zone of the package. The corresponding numerical and experimental results are shown, using a 4% convergence criterion, in Fig. 18, where the package was loaded with a new preparation of mashed potato $(57 - \jmath 28)$. The simulation time was 30 h and 32 min, while the total number of DOF was 686 882. The effects of thermal diffusion can be observed from the thermal image [see Fig. 18(b)].

A final configuration is considered where a thin-film sheet comprising a complex arrangement of antenna structures, shown in Fig. 19, is used to create a more uniform heating distribution in a low-loss food load $(4.1 - \jmath 0.42)$.

The normalized absolute electric field and consequent power density distribution when no thin-film surface is used, is shown in Fig. 20(a), for a convergence of 6.23%. A total of 278 471 DOF was used and the simulation time was 9 h and 9 min. The power density result highlights the nonuniform heating distribution within the asymmetrically positioned load geometry. When the patterned thin-film surface is placed on the load surface, the DOF are increased to 279 746. The hot spots are removed, as seen in Fig. 20(b), resulting in a more uniform heating pattern. The simulation required 9 h and 37 min to reach a convergence of 10.215%.

VII. CONCLUSION

The paper has presented a new 3-D edge element implementation of a discontinuous sheet for representing thin-film surfaces. This dual-surface formulation has been described for both the frequency- and time-domain FE methods. By comparison with three alternative boundary condition methods, the discontinuous sheet has been shown to yield results of superior accuracy. This is a consequence of including additional DOF in the set of unknown edge values, which account for the field discontinuity across a thin-film surface using standard transmission-line theory.

A hybrid discontinuous-resistive sheet element has also been introduced for linking split elements of the thin-film region with the surrounding mesh domain.

The use of the discontinuous sheet has been shown to be successful in characterizing the performance of modern microwave heating applications incorporating active package technologies [9].

ACKNOWLEDGMENT

The authors would like to acknowledge the assistance of Unilever Ltd., Sharnbrook, U.K., in providing active pack containers used for the validation of this study and to Dr. D. Dibben, Japanese Research Institute (JRI), Osaka, Japan, for many helpful discussions.

REFERENCES

[1] M. A. Leontovich, "On the approximate boundary conditions for electromagnetic fields on the surface of well conducting bodies," in *Investigations of Propagation of Radio Waves*, B. A. Vvdensky, Ed. Moscow, Russia: Academy of Sci. USSR, 1948, pp. 5–20.

[2] J. M. Jin, J. L. Volakis, C. L. Yu, and A. C. Woo, "Modeling of resistive sheets in finite element solutions," *IEEE Trans. Antennas Propagat.*, vol. 40, pp. 727–731, June 1992.

[3] F. Bocquet, L. Pichon, A. Razek, and G. Tanneau, "3-D FEM analysis of electromagnetic wave scattering from a dielectric sheet in EMC problems," *IEEE Trans. Magn.*, vol. 34, pp. 2791–2794, May 1998.

[4] S. Van den Berghe, F. Olyslager, and D. De Zutter, "Accurate modeling of thin conducting layers in FDTD," *IEEE Microwave Guided Wave Lett.*, vol. 8, pp. 75–77, Feb. 1998.

[5] M. Feliziani and F. Maradei, "Edge element analysis of complex configurations in presence of shields," *IEEE Trans. Magn.*, vol. 33, pp. 1548–1551, Feb. 1997.

[6] A. C. Metaxas, *Foundations of Electroheat: A Unified Approach*. New York: Wiley, 1996.

[7] F. Alessandri, G. Baini, G. D'Inzeo, and R. Sorrentino, "Conductor loss computation in multiconductor MIC's by transverse resonance technique and modified perturbational method," *IEEE Microwave Guided Wave Lett.*, vol. 2, pp. 250–252, June 1992.

[8] D. Dibben and A. C. Metaxas, "Frequency domain versus time domain finite element methods for calculation of fields in multimode cavities," *IEEE Trans. Magn.*, vol. 33, pp. 1468–1471, Feb. 1997.

[9] R. A. Ehlers, "Modeling of packaging systems in microwave fields," Ph.D. dissertation, Eng. Dept., Univ. Cambridge, Cambridge, U.K., 2001.

[10] W. Wood, *Practical Time Stepping Schemes*. Oxford, U.K.: Clarendon, 1990.

[11] D. Dibben and A. C. Metaxas, "Finite-element time-domain analysis of multimode applicators using edge elements," *J. Microw. Power Electromagn. Energy*, vol. 29, no. 4, pp. 242–251, 1994.

[12] C. Habeger, "Microwave interactive thin films," *Microwave World*, vol. 18, no. 1, pp. 8–22, 1997.

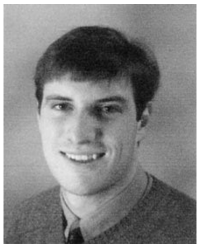

Richard A. Ehlers (M'96) was born in Johannesburg, South Africa, in 1975. He received the B.Sc. Eng. and M.Sc. Eng. degrees in electrical engineering from the University of the Witwatersrand, Witwatersrand, South Africa, in 1996 and 1998 respectively, and the Ph.D. degree from the Cambridge University, Cambridge, U.K., in 2001. His M.Sc. Eng. research concerned the prediction of large air-gap switching impulse breakdown voltages with an application to tower-conductor window configurations.

Since 1997, he has been a member of the Electricity Utilization Group, Cambridge University, Cambridge, U.K., involved with research into FE modeling of thin films for microwave heating applications. Upon completion of the Ph.D. degree, he continued his research on thin-film modeling, which has also been licensed to industry, as a Research Associate with the Engineering Department, Cambridge University. In addition to high-voltage and electromagnetics, his research interests include avionics, aerial navigation, and wireless communication systems. He is currently involved in the area of system analysis and process definition of new and converted aircraft with Airbus Industry.

A. C. Ricky Metaxas (M'91) received the Doctorate degree from Imperial College, University of London, London, U.K., in 1968.

He is a Fellow and Tutor with St. John's College, Cambridge, U.K. Besides his extensive teaching experience, he has been with the Atomic Energy Authority, the Electricity Council Research Centre (now EA Technology), and Eastern Electricity plc. From 1982 to 2002, he was seconded to the Engineering Department, University of Cambridge, Cambridge, U.K., where he founded and led the Electricity Utilization Group (EUG). He coauthored *Industrial Microwave Heating* (London, U.K.: Peregrinus, 1983), a book which is regarded as "the bible" for researchers working in the field of microwave heating. More recently, he authored the textbook *Foundations of Electroheat: A Unified Approach* (Chichester, U.K.: Wiley, 1996), which encompasses many aspects of electricity utilization from ohmic heating to laser welding. He has coauthored over 100 publications in many diverse areas such as electroheat, electricity utilization, modeling of industrial heating systems, and electromagnetics.

Dr. Metaxas is a Fellow of the Institution of Electrical Engineers (IEE), U.K., and is currently President of the Association of Microwave Power in Europe for Research and Education (AMPERE), a European-based organization devoted to the promotion of RF and microwave energy, for which he edits its newsletter.